Journal of Materials Chemistry C

Accepted Manuscript

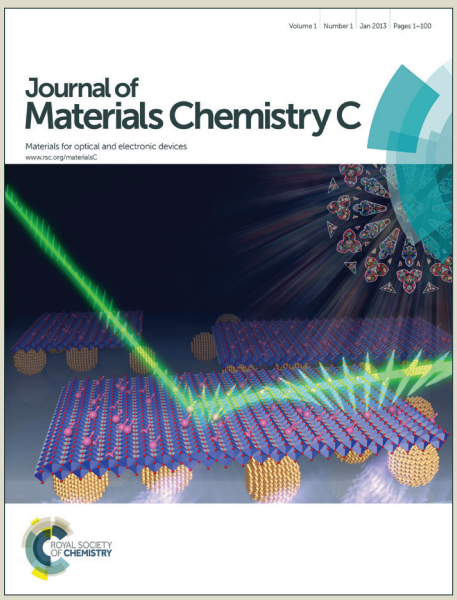

ROYAL SOCIETY OF CHEMISTRY

www.rsc.org/materialsC

Journal Name

RSCPublishing

ARTICLE

Direct synthesis of cobalt nanoparticles-imbedded mesoporous carbons for high-performance dye-sensitized solar cell counter electrodes

Cite this: DOI: 10.1039/xoxxoooooox

Received ooth January 2012,
Accepted ooth January 2012

DOI: 10.1039/xoxxoooooox

www.rsc.org/

Ming Chen,[a,#] Leng-Leng Shao,[a,#] Xing Qian,[b] Tie-Zhen Ren[c] and Zhong-Yong Yuan*[a]

Metal Co nanoparticles imbedded ordered mesoporous carbon (Co-OMC) materials are synthesized by a facile low-temperature hydrothermal approach of phenolic resin-F127 composites with various amounts of cobalt nitrate and subsequent carbonization. The synthesized Co-OMCs possess high BET surface area, uniform 2-D hexagonal ordered mesostructure and large pore volume, and the imbedded Co nanoparticles are homogeneously distributed with the size of 2-5 nm. In comparison with the pristine OMC, Co-OMCs exhibit higher graphitization degree, which is benefit to enhance the electrical conductivity. The Co-OMCs are applied as counter electrode catalysts in dye-sensitized solar cells (DSSCs), revealing that the electrocatalytic activity for the I_3^- reduction is improved due to the synergistic catalytic effect between OMC and the appropriate amount of Co nanoparticles, and the enhanced electrical conductivity. The DSSCs based on Co-OMC counter electrodes exhibit an optimum energy conversion efficiency of 7.02%, which is larger than that of the cell based on pure OMC counter electrode (6.18%), and comparable to that of the cell with Pt counter electrode (7.10%) under the same experimental conditions. High energy conversion efficiency, low cost and simple fabrication process make the Co-OMC counter electrode promising as an alternative for the replacement of the conventional Pt electrode in DSSC.

1. Introduction

To meet the demand for environmental-friendly and safe energy, one of most promising technologies is to convert solar energy directly into electricity using photovoltaic devices. Dye-sensitized solar cell (DSSC) is the most potential candidate for next-generation photovoltaic device and has been widely studied due to its low cost, easy fabrication and high power conversion efficiency.[1-3] A typical DSSC consists of a dye-sensitized nanocrystalline titanium dioxide (TiO_2) film, electrolyte containing iodide/triiodide (I^-/I_3^-) redox couples, and a counter electrode. As one of the crucial components in DSSC, the counter electrode (CE) collects electrons from the external circuit and catalyzes the reduction of triiodide ions for dye regeneration, which plays an important role in regulating the photovoltaic performance and stability of DSSC. Platinized FTO (fluorine-doped tin oxide) conducting glass electrode is commonly used as the CE in DSSC due to its good conductivity and excellent catalytic activity for the reduction of triiodide to iodide.[4, 5] However, the high cost of Pt and its limited reserve in the nature greatly restrict the practical application of DSSC, which has stimulated great efforts to seek low-cost and Pt-free CE. For an efficient CE, good electrocatalytic activity for the redox couples (such as I^-/I_3^-) and enhanced electrical conductivity for the transport of electrons are required. So far, a variety of materials including carbon materials,[6-8] conducting polymers,[9, 10] inorganic metal carbides,[11] sulfides[12] and nitrides[13, 14] have been investigated as CE catalysts in DSSCs, though few alternatives with comparable electrocatalytic activity to Pt CE in DSSCs are available. Thus it is still a challenge to develop low-cost and high-performance CE catalysts to replace the expensive Pt electrode in DSSCs.

Currently, many carbon materials such as carbon black, activated carbon, graphite, conductive carbon, carbon nanotube, carbon fiber and fullerene have been proven to be good CE candidates with superior electrocatalytic activity and stability.[15, 16] Among them, very recently ordered mesoporous carbons (OMCs) were specifically studied as the efficient CE catalysts due to their structural regularity for fast infiltration of electrolyte, high surface area for enhancement of effective

catalytic sites, good chemical stability and outstanding electrocatalytic activity.[17-19] Especially, amorphous OMC with graphitic pore walls is the potential efficient CE due to the enhanced electrical conductivity.[20] However, the common preparation of graphitic mesoporous carbon was implemented by high-temperature thermal treatment (~2500 ºC).[21, 22] This strategy not only increases the energy consumption, but deteriorates the pore structure. In contrast, catalytic graphitization by the assistance of metal salts (Fe, Ni etc.) at the lower temperature (< 1000 ºC) has attracted great attention.[23, 24] Thus, the development of graphitic mesoporous carbon with controlled textural properties by the feasible approach may be desirable for the high-performance CE electrocatalyst.

On the other hand, the incorporation of different nanosized inorganic metal compounds with tunable sizes, morphologies, and catalytic functions into mesoporous carbons created a new way for preparing highly catalytic CE materials for DSSCs.[25, 26] A series of transition-metal oxides, carbides and nitrides imbedded in mesoporous carbons have been prepared by in situ soft-template approach, and exhibited high power conversion efficiency surpassed the performance of the DSSC using traditional Pt CE,[11, 26, 27] suggesting their synergetic effects. However, to the best of our knowledge, little attention was concerned on the composites of transition metal (Ni, Co, etc.) nanoparticles and nanoporous carbons as electrocatalysts in DSSCs.

Undoubtedly, the composites of mesoporous carbons with embedded transition metal nanoparticles have been successfully fabricated through the hard-templating approach.[28, 29] Nevertheless, the multiple step process is time-consuming and complicated, and the resultant often displayed the disordered carbon framework and lower porosity. Moreover, the obtained metal nanoparticles are less uniform in size, often accompanying the severe aggregation. Therefore, developing more effective route to facilely synthesize graphitic ordered mesoporous carbon embedded with controllable and uniform metal nanoparticles may be highly proposed for their CE application.

Herein, a series of cobalt-imbedded OMCs (Co-OMCs) were prepared by the soft-templating approach based on the direct self-assembly of phenolic resins with F127 in the presence of $Co(NO_3)_2 \cdot 6H_2O$, and applied as CEs for DSSCs. The small-sized Co nanoparticles were embedded in the carbon matrices without causing the blockage of mesopores, simultaneously increasing the graphitization degree of the OMCs, and a protective layer from OMCs could be a good strategy to overcome the corrosion problems in the electrolyte. The resulting Co-OMCs as composite CE catalysts simultaneously provided high electrical conductivity and improved electrocatalytic activity, exhibiting superior photovoltaic performance of DSSCs with a higher energy conversion efficiency of 7.02% than that of the cell using OMC CE (6.18%), which is comparable to that of the one with Pt CE (7.10%) under the same experimental conditions.

2. Experimental section

2.1 Preparation of materials. Co-OMCs were synthesized by the slightly modified low-temperature autoclaving method.[30] 1.65 g of resorcinol and 2.5 g of F127 were dissolved in a mixture of 15 ml water and 15 ml ethanol, stirring for 15 min until the solution turned into colorless. 1, 2, or 4 g of $Co(NO_3)_2 \cdot 6H_2O$ dissolved in 10 ml of mixed solution of ethanol and water (volume ratio 1:1), together with 0.2 g of HCl (37 *wt*%), were added. After 1 h of stirring, 1.25 g of 37% formaldehyde solution was added dropwise. The reaction mixture was further vigorously stirred for another 1 h, and a homogeneous red solution was obtained, which was then transferred into a Teflon-lined autoclave and heated at 80 ºC for 2 days. The resulting polymer was washed with ethanol and water, dried in an oven at 60 ºC for 12 h. Carbonization was carried out in a tubular furnace under an inert atmosphere (N_2 flow) with a heating rate of 1 ºC/min, and then keeping the temperature at 800 ºC for 3 h. The final product was denoted as Co-OMC-*x* (*x* = 1, 2, 4), where *x* represents the added amount of cobalt nitrate. Ordered mesoporous carbon (OMC) was also prepared under the same condition without adding any of cobalt nitrate.

2.2 Preparation of counter electrodes. The FTO transparent glass substrates (14 Ω/□, Nippon Sheet Glass) were ultrasonically cleaned sequentially in detergent, acetone, ethanol and distilled water for 30 min, and then stored in ethanol before use. The Co-OMC-*x* or OMC CE was prepared as follows: 130 mg of Co-OMC-*x* or OMC and 15 mg of PEG-2000 were ultrasonically dispersed in 3 ml of deionized water and then continuously kept magnetic stirring for 2 h. Subsequently, TiO_2 colloid (20 mg, P25, Degussa) was dropped into the prepared pastes and stirred for 2 h continuously. Then the as-prepared slurry was scraped onto a FTO using the doctor blade method and dried at 100 ºC overnight. Pt CE was fabricated by conventional thermal decomposition of 30 mM $H_2PtCl_6 \cdot 6H_2O$ solution spin-coated on the surface of FTO at 400 ºC for 30 min.

2.3 Fabrication of DSSCs. The TiO_2 photoanode was prepared by the modified method.[31, 32] In brief, FTO was immersed in 50 mM $TiCl_4$ aqueous solution at 70 ºC for 30 min. Subsequently, the 20 nm-sized TiO_2 layer was coated onto the blocking layer using the doctor blade method and then sintered at 125 ºC for 30 min in air, resulting in a TiO_2 film with the thickness of *ca.* 6 μm. The 200 nm-sized TiO_2 was then printed on the FTO and sintered at 450 ºC for 30 min to obtain a light-scattering layer of *ca.* 3 μm in thickness. The double-layer TiO_2 films were finally treated with $TiCl_4$ aqueous solution, recalcined at 450 ºC for 30 min and cooled to room temperature. For the dye-sensitized TiO_2 film, the two layers of TiO_2 films were immersed into a 0.3 mM N719 dye (Solaronix SA, Switzerland) ethanol solution at room temperature for one night. The DSSCs were composed of a photoanode electrode, a counter electrode and an electrolyte containing 0.05 M I_2, 0.5 M LiI, 0.3 M 1,2-dimethyl-3-propylimidazoliumiodide (DMPII), and 0.5 M 4-tert-butylpyridine with acetonitrile as the

solvent. The 50 μm thick scotch tape was used as the spacer between the two electrodes.

2.4 Characterization. Powder X-ray diffraction (XRD) patterns were recorded on a Bruker D8 Focus diffractometer, with Cu K_α radiation (λ = 1.5406 Å) at 40 mA and 40 kV. Transmission electron microscopy (TEM) measurements were performed on a JEOL JEM 2010 microscope at 200 kV. All samples subjected to TEM measurements were ultrasonically dispersed in ethanol and drop-casted onto copper grids covered with carbon film. Nitrogen adsorption-desorption isotherms were measured on a Quantachrome NOVA 2000e sorption analyzer at 77 K. The samples were degassed in a vacuum at 200 ºC overnight prior to the measurement. The specific surface area (S_{BET}) was calculated by the Brunauer-Emmett-Teller (BET) method, the pore size distributions were derived from the adsorption branches of isotherms using BJH method, and the total pore volumes (V_{total}) were estimated from the adsorbed amount at a relative pressure P/P_0 of 0.980. Thermogravimetric analysis (TGA) curves were recorded on a TA SDT Q600 analyzer under a constant air flow of 100 ml min^{-1} with a heating rate of 10 K min^{-1}. Raman spectroscopy was performed on a Renishaw-1000 Raman spectrometer.

2.5 Electrochemical measurements. All photocurrent density-voltage tests of DSSCs were carried out under illumination of 100 mW cm^{-2} (AM 1.5) from a solar simulator (Oriel Sol 2A, Newport), calibrated by a standard silicon solar cell (Oriel Instrument). The cell active area used for the *J–V* measurements was 0.20 cm^2. Cyclic voltammetry (CV) measurement was conducted using the three-electrode system in acetonitrile solution containing 10 mM LiI, 1 mM I_2 and 0.1 M $LiClO_4$. The as-prepared electrode was served as working electrode, Pt/FTO as auxiliary electrode and Ag/Ag^+ electrode as reference electrode. The geometric area of the cells was 0.25 cm^2 and they were investigated with a potential scanning range of -1.0 V to 1.5 V at a scanning rate of 50 mV s^{-1}. Electrochemical impedance spectroscopy (EIS) and Tafel measurements were conducted on a Zahner Zennium impedance analyzer using the symmetric dummy cells. The EIS was conducted at -0.60 V bias with the frequency range of 100 kHz to 100 mHz. The amplitude of the sinusoidal AC modulation signal was 10 mV. Tafel polarization measurements were performed at a scan rate of 10 mV s^{-1}.

3. Results and discussion

The composites of Co nanoparticles embedded graphitic ordered mesoporous carbons were directly synthesized using resol as a carbon precursor, triblock copolymer F127 as mesostructure template, and cobalt nitrate as metal Co source. The synthesis strategy is illustrated in Scheme 1. Firstly, the soluble amphiphilic F127 produced the well-formed surfactant micelles in an ethanol/water solution, serving as the structure directing agent. Then the EO units of F127 interacted with the hydroxyl groups of resorcinol and $[Co(H_2O)_6]^{2+}$ complexes via hydrogen bonding, forming the $[Co(H_2O)_6]^{2+}$ surrounded hexagonally arranged F127 micelles[33, 34, 35]. Moreover, the polymerization between the formaldehyde and resorcinol in the acidic system produced the carbon precursor. By the hydrothermal treatment, the F127, $[Co(H_2O)_6]^{2+}$ complexes, and resorcinol-formaldehyde resols assembled into the composites of F127/Co^{2+}/resorcinol-formaldehyde copolymer, in which the Co^{2+} was well distributed. Carbonization of the composites at 800 ºC led to the removal of F127 and the reduction of Co^{2+} to Co as well as the catalytic graphitization of OMC. Finally the Co nanoparticles embedded graphitic ordered mesoporous carbon was formed.

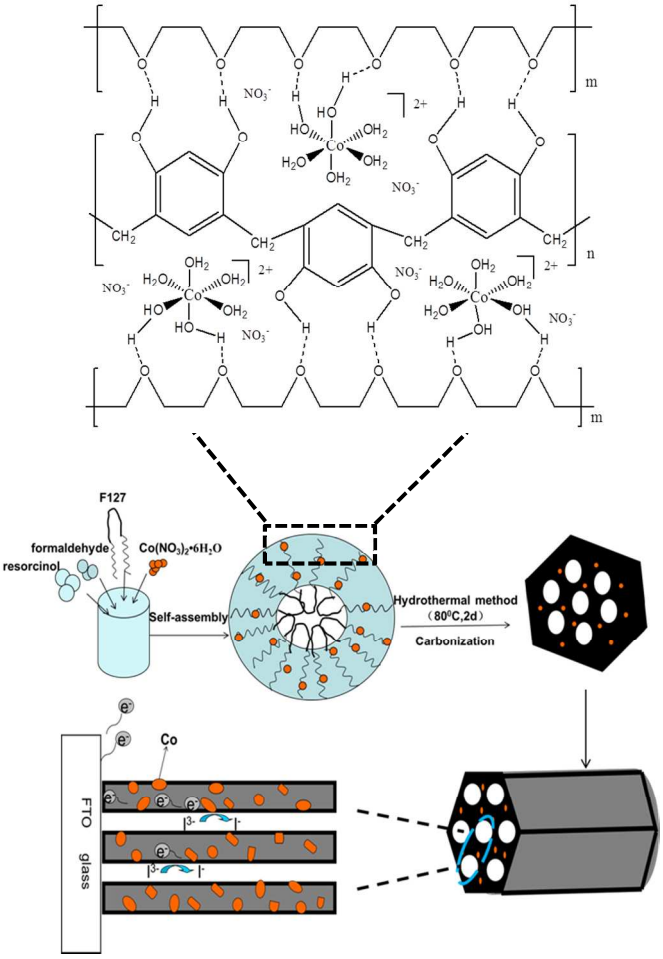

Scheme 1. The illustration for the preparation and application of Co-OMC-*x* as counter electrode in DSSCs.

Figure 1 shows both the small-angle and wide-angle XRD patterns of the Co-OMCs and the OMC samples. The OMC displayed a sharp and intense diffraction peak at 0.78º (2θ), which can be indexed as (100) reflection of an ordered 2-D hexagonal mesostructure.[30, 33] This single diffraction peak is also presented in the Co-OMCs, though the intensity decreased with the increase of the cobalt amount, accompanied with the shift of the diffractions to 2θ = 0.90°. This indicates that the structural mesopore ordering gradually degenerates and the pore size decreases with the increase of the Co content, suggesting that an appropriate amount of Co is favorable to retain the ordered mesostructure in Co-OMCs. As shown in

Figure 1b, OMC shows a typical broad diffraction peak at 23.04º (2θ), revealing the characteristics of amorphous carbon. However, as to Co-OMC-*x*, it is interesting that this diffraction peak moves to a larger 2θ with the increase of the Co content. Especially, an obvious diffraction peak at 2θ = 26.00º is displayed in Co-OMC-4 sample, which can be assigned to the (002) diffraction for typical graphite-like carbon. This demonstrates that there is a partial graphitization of the carbon in Co-OMC-*x* samples, and the Co loading efficiently enhanced the graphitization degree of OMCs.[23] Furthermore, all the Co-OMCs display relatively weak diffraction peaks at 2θ = 44.22º, 51.52º and 75.85º, which can be indexed to (111), (200) and (220) reflections of face-centered cubic cobalt (JCPDs card number 15-0806), suggesting the well crystallized Co nanoparticles in the carbon matrix. The average crystallite size of cobalt was calculated by the Scherrer's equation (D = 0.89k/βcosθ) from the integral breadth β of the strongest and well-resolved reflection peak [111] crystallographic direction. The corresponding average crystallite sizes for Co-OMC-1, Co-OMC-2 and Co-OMC-4 were *ca*. 3.5, 4.2 and 25.6 nm. No diffractions concerning cobalt carbide or cobalt oxide were detected, suggesting that Co^{2+} was reduced to Co during carbonization at 800 ºC under N_2 atmosphere.

To further investigate the structure of the synthesized Co-OMC-*x*, TEM was carried out and shown in Figure 2. For the OMC, the typical stripe-like and honeycomb-like pore arrangements confirm its well-ordered hexagonal mesostructure.

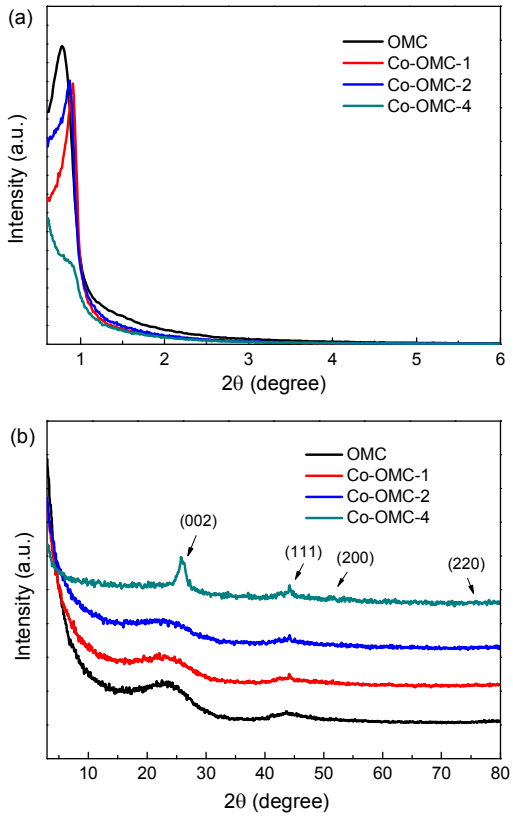

Figure 1. Low-angle (a) and wide-angle (b) XRD patterns of Co-OMC-*x* and OMC.

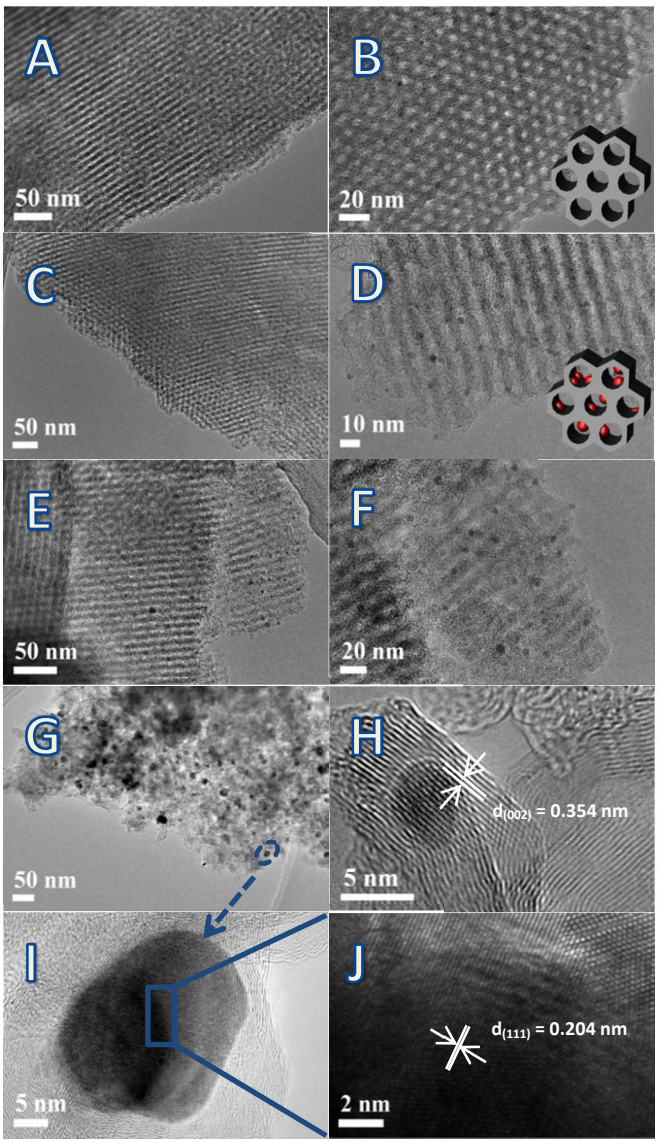

Figure 2. TEM images of OMC (A, B), Co-OMC-1 (C, D), Co-OMC-2 (E, F), Co-OMC-4 (G, H) and embedded Co nanoparticles in Co-OMC-4 (I, J).

The similar hexagonal mesostructures can also be clearly observed on the Co-OMC-1 and Co-OMC-2 samples, presenting the stripe-like channels with *d*-spacing of about 10.5 and 11.2 nm, respectively. While the Co nanoparticles with sizes ranging from 2 to 5 nm are highly dispersed in the carbon network of Co-OMC-1 and Co-OMC-2 samples. It can be seen that a part of Co nanoparticles are homogeneously inserted into the mesopore walls, and partially exposed in the mesopore channels. However, as to the sample Co-OMC-4, the mesochannels presented relatively low order with partially wormhole-like pore system due to the excessive Co nanoparticles, and the size of Co nanoparticles increased to tens nanometers, much larger than the average mesopore diameter of 4.18 nm. The measured lattice pitch d_{111} for Co in Co-OMC-4 was about 0.204 nm. It is suggested that the size of Co nanoparticles are dependent on the Co^{2+} concentration. At low Co^{2+} concentration, $Co(H_2O)_6^{2+}$ complex can homogeneously

distributed into the copolymer through moderately interacting with the EO units of F127 and without interrupting the self-assembly process. Upon carbonization, the spatial confinement effect from mesoporous carbon skeleton restricts the growth and aggregation of cobalt nanoparticles, resulting in well dispersed and small-sized nanoparticles. Nevertheless, the high Co^{2+} concentration not only weakened the hydrogen bonding between the EO units of F127 and phenolic resin leading to the low ordered OMC, but also contributed to the aggregated large-sized Co nanoparticles. Thus, appropriate precursor Co^{2+} concentration is crucial for the generation of ordered mesoporous structure and well dispersed cobalt nanoparticles. On the other hand, the graphitic carbon is obviously observed in the Co-OMC-*x* catalyst, in which the graphitization led to the formation of relatively large graphite crystallites with interlayer spacing of *ca*. 0.354 nm and the percentage of graphitic domains exhibits the increasing trend with the increase of Co content. This demonstrates that the pore structures of Co-OMCs slightly change from good mesopore ordering to relatively poor ordering with the increase of the Co loading, accompanying with the enhanced graphitization degree.

N_2 adsorption-desorption isotherms and the pore size distributions of the Co-OMC-*x* and OMC are presented in Figure 3, and the corresponding textural properties are summarized in Table 1. The OMC shows typical type IV isotherms with well-defined H1 type hysteresis loop, characteristic of mesoporous structure.[30] As for the Co-OMC-1 and Co-OMC-2, the isotherms still remain the similar shapes, suggesting the retaining of well-defined mesostructure after loading small amount of Co. While for the Co-OMC-4, the isotherms changed with the reduced nitrogen uptake, accompanying with H2 type hysteresis loop, suggesting the destruction of ordered mesostructure due to the introduction of excessive Co nanoparticles into the carbon network. Correspondingly, the BJH pore size distributions of OMC, Co-OMC-1, Co-OMC-2 and Co-OMC-4 centered at 6.45, 5.83, 5.85 and 4.18 nm, respectively, exhibiting the tendency that the higher Co loading resulted in the smaller pore diameter. As seen from Table 1, with the increase of the Co content in Co-OMC-*x*, the BET surface area decreased from 719 to 417 m^2g^{-1}, and the pore volume from 0.71 to 0.40 cm^3g^{-1}, revealing that the partial damage of ordered mesostructure and blockage of mesopores with the increase of Co nanoparticles embedded in carbon matrices. However, Co-OMC-1 and Co-OMC-2 with appropriate amount of Co loading still possess a large surface area and pore volume of 676 - 649 m^2g^{-1} and 0.65 - 0.50 cm^3g^{-1}, respectively. The observed high surface area and appropriate pore size for Co-OMC-1 and Co-OMC-2 are of great significance for the reduction and diffusion of triiodide.[18]

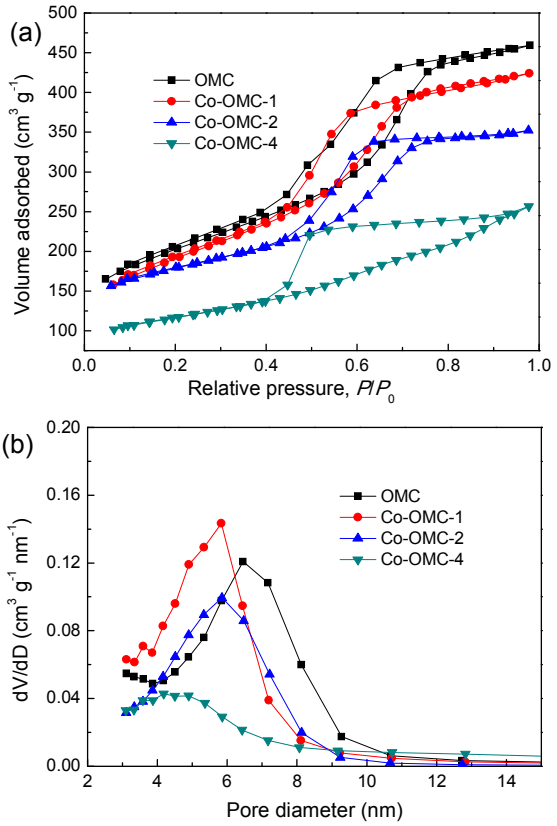

Figure 3. (a) N_2 adsorption-desorption isotherms of Co-OMC-*x* and OMC and (b) their corresponding pore size distribution curves.

To quantificationally analyze the content of Co nanoparticles in the Co-OMC-*x* composites, TG was performed in an air stream from 30 to 800 ºC (Figure 4). As shown in Figure 4a, weight loss of samples below 200 ºC is due to the dehydration reaction and the weight loss between 200 and 650 ºC should be ascribed to the oxidation of Co and carbon. In the range of 200 – 650 ºC, the exothermic peaks (Figure 4b) at 605, 618, 597 and 540 ºC were observed for the OMC, Co-OMC-1, Co-OMC-2 and Co-OMC-4, respectively, which are due to the oxidation of carbon in the air atmosphere. The shift of the

Table 1. Structural and Textural Properties of Co-OMC-*x* and OMC

Sample	I_D/I_G	Co size (nm)	Co mass (*wt*%)	S_{BET} [a] (m^2g^{-1})	S_{micro} [b] (m^2g^{-1})	V_{total} (cm^3g^{-1})	V_{micro} [b] (cm^3g^{-1})	D_{DFT} [c] (nm)	D_{BJH} [d] (nm)	d_{100} [e] (nm)	a_0 [e] (nm)	t [f] (nm)
OMC	2.08	---	0	719	225	0.71	0.10	4.64	6.45	11.3	13.0	6.6
Co-OMC-1	2.00	3.5	2.0	676	169	0.65	0.07	4.15	5.83	9.8	11.3	5.5
Co-OMC-2	1.89	4.2	3.0	649	317	0.55	0.13	4.40	5.85	10.2	11.8	6.0
Co-OMC-4	1.67	25.6	4.3	417	185	0.40	0.08	3.79	4.18	9.8	11.3	7.1

[a] The BET surface area S_{BET} calculated using adsorption data in a relatively pressure range $P/P_0 = 0.05–0.24$. [b] The micropore surface area S_{micro} and the micropore volume V_{micro} estimated by the *t*-plot method. [c] The pore diameter D_{DFT} obtained from the maxima of the pore size distribution curve by the DFT method. [d] The pore size D_{BJH} obtained from the maxima of the pore size distribution curve calculated by the BJH method. [e] The d-spacing of the (100) diffraction $d_{(100)}$, and unit cell parameter a_0 calculated from the XRD patterns by $a_0 = 2d_{(100)}/\sqrt{3}$. [f] Pore wall thickness calculated as thickness $t = a_0 - D_{BJH}$.

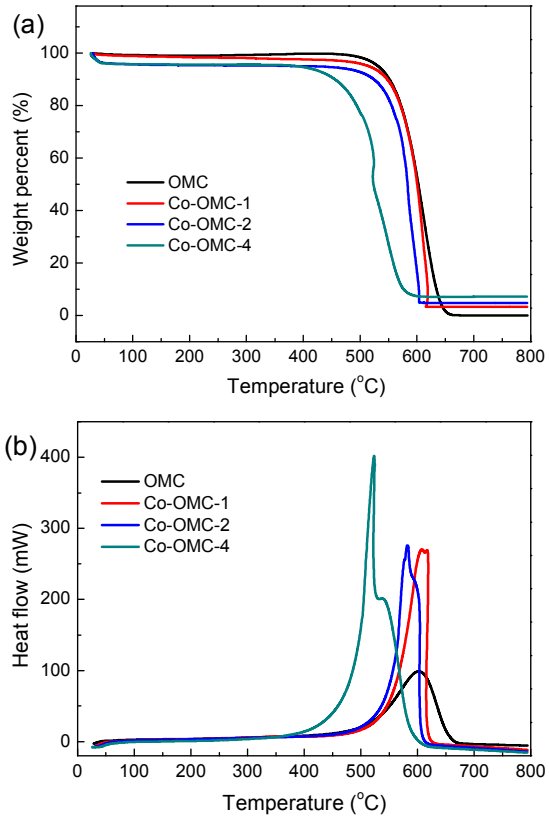

Figure 4. Simultaneous (a) TG and (b) DSC curves of Co-OMC-*x* and OMC.

carbon oxidation peak to a lower temperature suggests the thermal stability slightly decreased with the increase of Co loading. Meanwhile the exothermic shoulder peaks located at the temperatures of 607, 582 and 523 ºC are belonged to the oxidation of Co in the Co-OMC-1, Co-OMC-2 and Co-OMC-4, respectively. The temperature of the exothermic shoulder peaks of Co is lower than that of carbon, indicating the Co nanoparticles are easier to be oxidized into Co_3O_4 nanoparticles. The Co content (x%) is calculated by subtracting the oxygen content from the Co_3O_4 residue content according to the eq. 1,

$$x\% = \frac{m_2 M_{Co}}{m_1 M_{Co_3O_4}} \times 100\% \quad (1)$$

where m_1 and m_2 are the mass of Co-OMC-*x* composites and residual Co_3O_4 nanoparticles, respectively. M_{Co} and Mco_3o_4 are the molecular weight of Co and Co_3O_4, respectively. Since the mass percentage of residual Co_3O_4 is 2.7%, 4.1% and 5.9% for Co-OMC-1, Co-OMC-2 and Co-OMC-4 composites, their calculated Co content is 2.0, 3.0, 4.3 *wt*%, respectively.

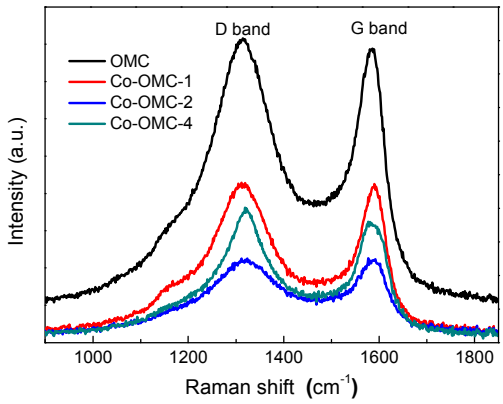

Figure 5. Raman spectra of Co-OMC-*x* and OMC.

Raman spectroscopy measurement is also a powerful tool to further study the structure of Co-OMC-*x*. As shown in Figure 5, the Raman spectra of all samples show two broad peaks at about 1318 and 1591 cm^{-1}, corresponding to the disordered carbons (D-band) and the graphitized carbons (G-band), respectively. It is well known that the relative intensity ratio of I_D/I_G is a measure of the graphitization degree.[24, 36] The corresponding I_D/I_G ratios of OMC, Co-OMC-1, Co-OMC-2 and Co-OMC-4 are 2.08, 2.00, 1.89 and 1.67, respectively, indicating the graphitization was enhanced in the presence of Co nanoparticles, and the graphitization degree indeed enhanced along with the increase of Co loading. Especially, the Co-OMC-4 possesses fine graphite crystallites resulting from the large graphitization degree of amorphous carbons.[37] These features are well consistent with wide-angel XRD patterns (Figure 1) and TEM images (Figure 2).

With regard to the targeted application of the counter electrodes in DSSCs, the Co-OMC-*x* composites with high surface area, ordered mesoporous channels and enhanced electrical conductivity are investigated. For comparison, the pristine OMC and pure Co particles (*ca.* 75 μm in size) were also examined as CEs. Figure 6 shows the performance of DSSCs using different CEs, and the detailed photovoltaic parameters of these cells are listed in Table 2. It can be obviously seen that the power conversion efficiency (η) of DSSCs based on the Co-OMC-1 (7.02%) and Co-OMC-2 (6.84%) electrodes is much higher than that of the cell using pristine OMC (6.18%) CE. Meanwhile, the DSSC with pristine Co CE gives a η of 0.87%, suggesting a certain catalytic activity of Co in the reduction of triiodide. Thus, the improvement of photovoltaic performance for the cells with Co-OMC-1 and Co-OMC-2 CEs can be attributed to the following aspects (Scheme 1). Primarily, the retained highly ordered mesoporous structure in the Co-OMC-1 and Co-OMC-2 arising from the good self-assembly between the phenolic resin and F127 is beneficial for the fast diffusion of triiodide,[19] increasing the reduction rate of I_3^- to I^-. Secondly, the increased electrical conductivity can further improve the transportation capacity of the electron back from the external circuit based on their enhanced graphitization degree after the

modification of Co nanoparticles. Finally, a suitable amount of Co nanoparticles embedded in the mesopores or pore walls may play a certain role in the catalytic reduction of triiodide.[38] Notably, the DSSCs using Co-OMC-1 and Co-OMC-2 electrodes even display comparable short-circuit photocurrent (J_{sc}) and open-circuit photovoltage (V_{oc}) to those of Pt electrode, indicating their excellent electrocatalytic activity for the reduction of triiodide ions. Particularly, the DSSC using Co-OMC-1 electrode shows the optimized photovoltaic performance (J_{sc} = 17.98 mA cm^{-2}, V_{oc} = 0.709 V, FF = 0.55) with a maximum η of 7.02%, which is comparable to that of the conventional Pt electrode (7.10%) under the same experimental conditions. However, for the Co-OMC-4 sample, the excessive Co nanoparticles are embedded in the carbon framework, leading to the damage of ordered mesopore structure and the decrease of specific surface area. The unfavorable structure slows down the ions diffusion and reduces available active sites, resulting in the relatively poor photovoltaic performance compared with those of Co-OMC-1 and Co-OMC-2 electrodes, though the large-scale graphitic carbon increased the transportation rate of electrons.

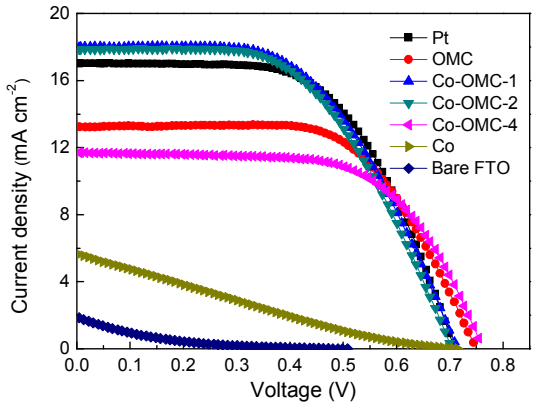

Figure 6. Photocurrent-voltange curves (*J-V*) of the DSSCs with different counter electrodes.

Table 2. Photovoltaic and electrochemical parameters of the DSSCs with different counter electrodes

Counter electrode	R_s (Ω)	R_{ct} (Ω)	J_{sc} (mA cm^{-2})	V_{oc} (V)	FF	η (%)
Pt	32.13	15.36	17.01	0.709	0.59	7.10
OMC	30.45	30.50	13.23	0.745	0.63	6.18
Co-OMC-1	29.96	10.10	17.98	0.709	0.55	7.02
Co-OMC-2	30.43	12.36	17.86	0.700	0.55	6.84
Co-OMC-4	29.98	46.93	11.69	0.754	0.63	5.57
Co	28.23	405.61	5.63	0.713	0.22	0.87
Bare FTO	-	-	1.85	0.510	0.11	0.10

In fact, the triiodine reduction reaction on the electrocatalyst surface could be influenced by these crucial factors, such as electron transport, electrolyte diffusion and catalytically active site. The optimum catalytic activity should be built on a good balance between these factors. As revealed by the above XRD, TEM, nitrogen adsorption analysis and Raman spectra, it is seen that, in comparison with the graphitic carbon, amorphous carbon material possesses a larger amount of the catalytic active sites or the defective sites due to its amorphous structure, however, the amorphous structure commonly leads to the poor electrical conductivity, thus decreasing the transportation rate of electrons. The amorphous carbon modified by the appropriate amount of Co nanoparticles can not only enhance the electrical conductivity arising from the improved graphitization, but also maintain abundant catalytic sites. Furthermore, the Co nanoparticles embedded in the carbon network provide the additional catalytic sites to assist the OMC for the reduction of triiodide. Both the enhanced electrical conductivity and abundant catalytic sites make the Co-OMC-1 and Co-OMC-2 achieve excellent electrocatalytic activities for the triiodide reduction, thus resulting in the good performance of DSSCs based on the Co-OMC-1 and Co-OMC-2 CEs. Nevertheless, the introduction of excessive Co nanoparticles into the carbon framework leads to the remarkably decrease of defective sites and disordered mesoporous channels due to the emergence of large-scale graphitic carbon.[23] The significant decrease of defective sites and slow electrolyte diffusion cannot be compensated by the enhanced electrical conductivity, thus leading to the inferior catalytic activity of Co-OMC-4 and poor performance of DSSC using Co-OMC-4 CE.

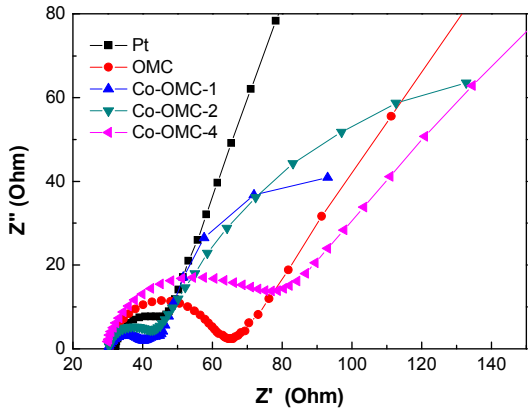

Figure 7. EIS spectra of the symmetric cells with two identical electrodes.

To gain insight into the electrocatalytic activity of various CEs for the reduction of triiodide，EIS was measured in a symmetric cell configuration consisting of two identical electrodes.[17] The obtained Nyquist plots are shown in Figure 7 and the corresponding parameters are summarized in Table 2. In a typical Nyquist plot, the intercept on the real axis at high frequency around 100 kHz represents the series resistance (R_s), including both the sheet resistance of the FTO glass substrate and the contact resistance of the counter electrode.[25] The semicircle in the high-frequency region arises from the charge-transfer resistance (R_{ct}) and the corresponding constant phase angle element (CPE) at the electrode/electrolyte interface, while the beeline in the low-frequency range represents the Warburg diffusion resistance (R_{diff}) of the I^-/I_3^- redox couple in the electrolyte.[39] The R_{ct}, a direct measure of the intrinsic electrocatalytic activity of an electrode, is well accepted to be

low in high-efficiency DSSCs.[26, 40] The Co-OMC-1 and Co-OMC-2 exhibit low charge transfer resistance of 10.10 and 12.36 Ω, respectively, which are lower than those of OMC (30.50 Ω), Co (405.61 Ω) and Pt (15.36 Ω), highlighting an excellent catalytic activity. The superior catalytic activity may confirm the advantages of the unique structure of Co-OMC-1 and Co-OMC-2 on the triiodide reduction. On one hand, highly ordered mesoporous system provides fast ion transport network and appropriate graphitization degree is favorable for the electron transportation. On the other hand, certain synergistic effect between highly dispersed Co nanoparticles and OMC can greatly lower the electron transfer resistance, resulting in a significant improvement of the catalytic activity. However, the large charge transfer resistance was observed in Co-OMC-4, suggesting the relatively lower catalytic activity for the triiodide reduction. The poor property may be attributed to the collapse of the partial mesoporous channels and the reduction of defective sites as well as the aggregation of Co nanoparticles which caused the inferior catalytic activity and a large R_{ct}. The EIS results are in good accordance with the photocurrent-voltage experiments.

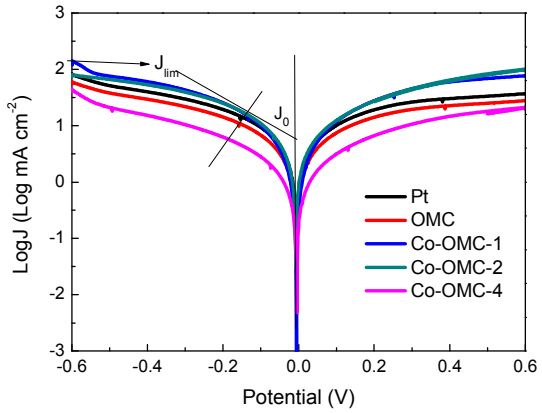

Figure 8. Tafel plots of symmetrical cells based on the Co-OMC-*x*, OMC and Pt electrodes.

Tafel polarization measurements were carried out to further study the interfacial charge-transfer properties on the electrode surface.[41] Figure 8 shows the Tafel curves of Co-OMC-*x*, OMC and Pt CEs. The exchange current density (J_0) is an important parameter which is closely related to the catalytic activity of the catalyst, and it can be obtained from the intersection of the cathodic branch and the equilibrium potential line.[11] The curves of Co-OMC-1 and Co-OMC-2 exhibit large exchange current densities which are higher than that of the pristine OMC CE, implying lower charge-transfer resistances at the electrolyte-electrode interface and superior catalytic activities for I_3^- reduction. Even, the exchange current densities of Co-OMC-1 and Co-OMC-2 CEs are slightly higher than that of Pt CE, demonstrating that they can act highly efficient electrocatalysts as Pt. In contrast, Co-OMC-4 gives a low J_0, indicating that it cannot perform as effectively as Co-OMC-1, Co-OMC-2 and Pt. Moreover, J_0 is also closely associated with the R_{ct} value as displayed in eq. 2.[25]

$$J_0 = \frac{RT}{nFR_{ct}} \quad (2)$$

The order of R_{ct} obtained from eq. 2 is in good agreement with the EIS tests. On the other hand, J_{lim} is another important parameter which is determined by the diffusion properties of the redox couple and the CE catalysts according to eq. 3,

$$D = \frac{l}{2nFC} J_{lim} \quad (3)$$

where R is the gas constant, D is the diffusion coefficient of the triiodide, l is the spacer thickness, T, R_{ct}, F and n have their usual meaning. The J_{lim} values of Co-OMC-1 and Co-OMC-2 electrodes are larger than those of the Pt and OMC electrodes, which means larger diffusion coefficients due to the well-defined and beneficial mesostructure.[42] The much lower J_{lim} of Co-OMC-4 compared to that of Co-OMC-1 and Co-OMC-2, further confirming that the relatively poor mesoporous structure destroyed the diffusion of electrolyte ions and the aggregation of Co nanoparticles weakened the synergistically catalytic activity.

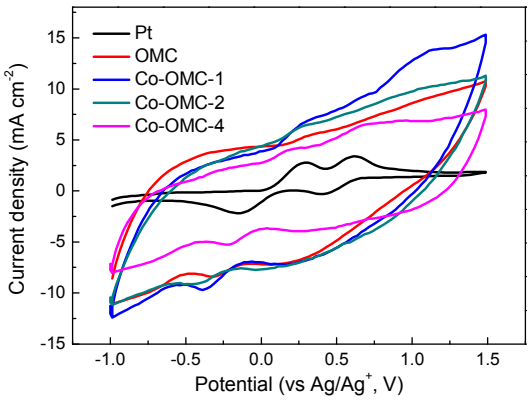

Figure 9. Cyclic voltammograms of various counter electrodes.

CV is another important tool to examine the catalytic activity of a counter electrode for the reduction of triiodide. It is well known that the cathodic current density depends on the scan rate of CV measurement.[43] In this work, CV curves of various counter electrodes were obtained at a scan rate of 50 mV s^{-1} and shown in Fig. 9. As for Pt electrode, two pairs of redox peaks are clearly observed, in which the left pair in the low potential range corresponds to redox reaction 4 and the right pair in the high potential range corresponds to redox reaction 5.[44]

$$I_3^- + 2e \leftrightarrow 3I^- \quad (4)$$

$$3I_2 + 2e \leftrightarrow 2I_3^- \quad (5)$$

Only one pair of redox peaks assigned to redox reaction 4 is observed for Co-OMC-*x* and OMC. Since the reduction process of triiodide ions in the redox reaction 4 is the rate-determining step for electron transfer from the counter electrode to the electrolyte,[45] it is necessary to investigate the reduction process of triiodide from the CV curves. It can be noted that the reduction peaks of Co-OMC-*x* and OMC are more negative

than that of Pt electrode, suggesting a more irreversible process for the triiodide reduction. Notably, the Co-OMCs and OMC electrodes exhibit much higher background current densities compared with that of Pt electrode, which mainly results from the double-layer capacitance on the interface of electrode/electrolyte due to the effective diffusion and adsorption of I_3^- on the large surface area. This phenomenon may promote their electrocatalytic activity toward the I_3^- reduction. Besides, compared to that of pristine OMC electrode, the reduction peak current densities of Co-OMC-1 and Co-OMC-2 are slightly larger, implying their enhanced electrocatalytic activity for the reduction of triiodide. However, Co-OMC-4 displays the much smaller current density than Co-OMC-1 and Co-OMC-2, due to its higher graphitization degree that reduces the catalytic sites of amorphous carbon and its disordered mesoporous channels that are unfavorable to the electrolyte diffusion. On the basis of the aforementioned CV, EIS and Tafel results, the Co-OMC-1 and Co-OMC-2 CEs with corresponding Co contents of 2.0 and 3.0 *wt*% show an excellent catalytic activity toward the I_3^- reduction, well explaining the good photovoltaic performance of the cells.

4. Conclusions

Co-OMC-*x* composites were fabricated by a one-pot organic-organic self-assembly strategy of phenolic resin and F127 in the presence of cobalt nitrate and subsequent carbonization. Metal cobalt nanoparticles were homogenously imbedded in the carbon network, accompanying with the enhanced graphitization degree and the well-organized mesostructure. Based on the enhanced graphitization degree, high surface area, and highly oriented mesostructure of Co-OMC-*x* counter electrodes, the Co-OMC-*x* DSSCs showed higher energy conversion efficiencies than the pristine OMC one. The optimized conversion efficiency of the cell with Co-OMC-1 CE (7.02%) is even comparable to that of the one using Pt counter electrode (7.10%). It is demonstrated that Co-OMC-*x* with appropriate Co content can significantly improve the electrocatalytic activity of OMC, due to the synergistic catalytic effect and enhanced electroconductivity owing to the suitable graphitization degree. The present simple fabrication method of Co-OMC-*x* not only provides a novel and low-cost pathway to develop Pt-free counter electrode material for the large-scale application of DSSCs, but also can be extended to the synthesis of other metal imbedded ordered mesoprous carbon materials as efficient counter electrode catalysts.

Acknowledgements

This work was supported by the National Natural Science Foundation of China (21076056 and 21073099), the Specialized Research Fund for the Doctoral Program of Higher Education (20110031110016), the Program for Innovative Research Team in University (IRT13022), the 111 project (B12015), and the Key Laboratory of Advanced Catalytic Materials in Zhejiang Normal University (ZJHX201301).

Notes and references

[a] Key Laboratory of Advanced Energy Materials Chemistry (Ministry of Education), Collaborative Innovation Center of Chemical Science and Engineering (Tianjin), College of Chemistry, Nankai University, Tianjin 300071, China. E-mail: zyyuan@nankai.edu.cn.
[b] State Key Laboratory of Elemento-organic Chemistry, College of Chemistry, Nankai University, Tianjin 300071, China.
[c] School of Chemical Engineering and Technology, Hebei University of Technology, Tianjin 300130, China.
[#] These authors have made an equal contribution to this work.

1. B. O'Regan and M. Grätzel, *Nature*, 1991, **353**, 737-740.
2. T. Y. Ma, Y. S. Wei, T. Z. Ren, L. Liu, Q. Guo and Z. Y. Yuan, *ACS Appl. Mater. Interfaces*, 2010, **2**, 3563-3571.
3. N. L. Yang, J. Zhai, D. Wang, Y. S. Chen and L. Jiang, *ACS Nano*, 2010, **4**, 887–894.
4. N. Papageorgiou, W. F. Maier and M. Grätzel, *J. Electrochem. Soc.*, 1997, **144**, 876-884.
5. T.-L. Hsieh, H.-W. Chen, C.-W. Kung, C.-C. Wang, R. Vittal and K.-C. Ho, *J. Mater. Chem.*, 2012, **22**, 5550.
6. Y. Jo, J. Y. Cheon, J. Yu, H. Y. Jeong, C.-H. Han, Y. Jun and S. H. Joo, *Chem. Commun.*, 2012, **48**, 8057–8059.
7. S. Y. Jang, Y. G. Kim, D. Y. Kim, H. G. Kim and S. M. Jo, *ACS Appl. Mater. Interfaces*, 2012, **4**, 3500-3507.
8. G. Wang, W. Xing and S. Zhuo, *J. Power Sources*, 2009, **194**, 568-573.
9. Q. Tai, B. Chen, F. Guo, S. Xu, H. Hu, B. Sebo and X. -Z. Zhao, *ACS Nano*, 2011, **5**, 3795-3799.
10. L. Kavan, J. H. Yum and M. Grätzel, *ACS Nano*, 2011, **5**, 165–172.
11. M. Wu, X. Lin, Y. Wang, L. Wang, W. Guo, D. Qi, X. Peng, A. Hagfeldt, M. Grätzel and T. Ma, *J. Am. Chem. Soc.*, 2012, **134**, 3419-3428.
12. M. Wang, A. M. Anghel, B. Marsan, N. C. Ha, N. Pootrakulchote, S. M. Zakeeruddin and M. Grätzel, *J. Am. Chem. Soc.*, 2009, **131**, 15976–15977.
13. Q. W. Jiang, G. R. Li and X. P. Gao, *Chem. Commun.*, 2009, 6720.
14. G. R. Li, J. Song, G. L. Pan and X. P. Gao, *Energy Environ. Sci.*, 2011, **4**, 1680.
15. M. Wu and T. Ma, *J. Phys. Chem. C*, 2014, doi:10.1021/jp412713h.
16. Y.-S. Wei, Q.-Q. Jin and T.-Z. Ren, *Solid-State Electronics*, 2011, **63**, 76-82.
17. M. Chen, L. L. Shao, X. Qian, L. Liu, T. Z. Ren and Z. Y. Yuan, *Chem. Eng. J.*, 2014, **256**, 23-31.
18. B. Zhao, H. Huang, P. Jiang, H. Zhao, X. Huang, P. Shen, D. Wu, R. Fu and S. Tan, *J. Phys. Chem. C*, 2011, **115**, 22615-22621.
19. T. Peng, W. Sun, X. Sun, N. Huang, Y. Liu, C. Bu, S. Guo and X.-Z. Zhao, *Nanoscale*, 2013, **5**, 337.
20. D.-Y. Kang, Y. Lee, C.-Y. Cho and J. H. Moon, *Langmuir*, 2012, **28**, 7033-7038.
21. S. B. Yoon, G. S. Chai, S. K. Kang, J.-S. Yu, K. P. Gierszal and M. Jaroniec, *J. Am. Chem. Soc.*, 2005, **127**, 4188-4189.
22. M. N. Patel, X. Wang, D. A. Slanac, D. A. Ferrer, S. Dai, K. P. Johnston and K. J. Stevenson, *J. Mater. Chem.*, 2012, **22**, 3160.
23. L. Sun, C. Tian, Y. Fu, Y. Yang, J. Yin, L. Wang and H. Fu, *Chem. Eur. J.*, 2014, **20**, 564-574.
24. Y. Liu, Q. Liu, J. Gu, D. Kang, F. Zhou, W. Zhang, Y. Wu and D. Zhang, *Carbon*, 2013, **64**, 132-140.

25. M. Wu, X. Lin, A. Hagfeldt and T. Ma, *Angew. Chem. Int. Ed.*, 2011, **50**, 3520-3524.
26. E. Ramasamy, C. Jo, A. Anthonysamy, I. Jeong, J. K. Kim and J. Lee, *Chem. Mater.*, 2012, **24**, 1575-1582.
27. M. Wu, X. Lin, L. Wang, W. Guo, Y. Wang, J. Xiao, A. Hagfeldt and T. Ma, *J. Phys. Chem. C*, 2011, **115**, 22598-22602.
28. L. Tang, G.-D. Yang, G.-M. Zeng, Y. Cai, S.-S. Li, Y.-Y. Zhou, Y. Pang, Y.-Y. Liu, Y. Zhang and B. Luna, *Chem. Eng. J.*, 2014, **239**, 114-122.
29. H.-W. Liang, W. Wei, Z.-S. Wu, X. Feng and K. Müllen, *J. Am. Chem. Soc.*, 2013, **135**, 16002-16005.
30. L. Liu, F.-Y. Wang, G.-S. Shao and Z.-Y. Yuan, *Carbon*, 2010, **48**, 2089-2099.
31. J. H. Wu, S. C. Hao, Z. Lan, J. M. Lin, M. L. Huang, Y. F. Huang, L. Q. Fang, S. Yin and T. Sato, *Adv. Funct. Mater.*, 2007, **17**, 2645-2652.
32. J. H. Wu, Z. Lan, J. M. Lin, M. L. Huang, S. C. Hao, T. Sato and S. Yin, *Adv. Mater.*, 2007, **19**, 4006-4011.
33. C. Liang and S. Dai, *J. Am. Chem. Soc.*, 2006, **128**, 5316-5317.
34. Ö. Þelik and Ö. Dag, *Angew. Chem. Int. Ed.*, 2001, **40**, 3800-3803.
35. T.-Y. Ma, L. Liu and Z.-Y. Yuan, *Chem. Soc. Rev.*, 2013, **42**, 3977.
36. S. Zhang, L. Chen, S. Zhou, D. Zhao and L. Wu, *Chem. Mater.*, 2010, **22**, 3433-3440.
37. D. W. Zhang, X. D. Li, H. B. Li, S. Chen, Z. Sun, X. J. Yin and S. M. Huang, *Carbon*, 2011, **49**, 5382-5388.
38. J.-M. Yan, X.-B. Zhang, H. Shioyama and Q. Xu, *J. Power Sources*, 2010, **195**, 1091-1094.
39. G. Yue, J. Wu, Y. Xiao, M. Huang, J. Lin and J.-Y. Lin, *J. Mater. Chem. A*, 2013, **1**, 1495.
40. F. Gong, Z. Li, H. Wang and Z.-S. Wang, *J. Mater. Chem.*, 2012, **22**, 17321.
41. L. Wang, E. W.-G. Diau, M. Wu, H.-P. Lu and T. Ma, *Chem. Commun.*, 2012, **48**, 2600.
42. M. Wu, X. Lin, T. Wang, J. Qiu and T. Ma, *Energy Environ. Sci.*, 2011, **4**, 2308.
43. S.-Y. Tai, C.-J. Liu, S.-W. Chou, F. S.-S. Chien, J.-Y. Lin and T.-W. Lin, *J. Mater. Chem.*, 2012, **22**, 24753.
44. F. Gong, H. Wang, X. Xu, G. Zhou and Z. S. Wang, *J. Am. Chem. Soc.*, 2012, **134**, 10953-10958.
45. G. R. Li, F. Wang, J. Song, F. Y. Xiong and X. P. Gao, *Electrochim. Acta*, 2012, **65**, 216-220.